Depth-encoded optical coherence elastography for simultaneous volumetric imaging of two tissue faces

Qi Fang[1,2,†,*], Luke Frewer[1,2,†], Philip Wijesinghe[1,3], Wes M. Allen[1,3], Lixin Chin[1,2], Juliana Hamzah[4], David D. Sampson[3,5], Andrea Curatolo[1,2], and Brendan F. Kennedy[1,2]

[1]BRITElab, Harry Perkins Institute of Medical Research, QEII Medical Centre, 6 Verdun Street, Nedlands, WA 6009, Australia
[2]School of Electrical, Electronic & Computer Engineering, The University of Western Australia, 35 Stirling Highway, Perth, WA 6009, Australia
[3]Optical+Biomedical Engineering Laboratory, School of Electrical, Electronic & Computer Engineering, The University of Western Australia, 35 Stirling Highway, Perth, WA 6009, Australia
[4]Harry Perkins Institute of Medical Research, QEII Medical Centre, 6 Verdun Street, Nedlands, WA 6009, Australia
[5]Centre for Microscopy, Characterisation & Analysis, The University of Western Australia, 35 Stirling Highway, Perth, WA 6009, Australia
[†]Contributed equally as co-authors
[*]Corresponding author: qi.fang@uwa.edu.au

2017

Abstract

Depth-encoded optical coherence elastography (OCE) enables simultaneous acquisition of two three-dimensional (3D) elastograms from opposite sides of a sample. By choice of suitable path-length differences in each of two interferometers, detected carrier frequencies are separated, allowing depth-ranging from each interferometer to be performed simultaneously using a single spectrometer. We demonstrate depth-encoded OCE on a silicone phantom and a freshly excised sample of mouse liver. This technique minimizes the required spectral detection hardware and halves the total scan time. Depth-encoded OCE may expedite clinical translation in time-sensitive applications requiring rapid 3D imaging of multiple tissue surfaces, such as tumor margin assessment in breast-conserving surgery.

Optical coherence elastography (OCE) [1] refers to a suite of techniques used to form images of a mechanical parameter of tissue on the micro-scale. OCE utilizes optical coherence tomography (OCT) to measure the deformation of a sample under mechanical loading. The measured deformation is used to generate images (in two or three dimensions) of a mechanical parameter, *e.g.*, strain, or alternatively, an estimate of an absolute mechanical property, *e.g.*, elastic modulus [2, 3].

The resolution of OCE, 10s-100s μm [2], lies between that of cellular-scale mechanical imaging techniques, such as atomic force microscopy (AFM) [4], and clinical techniques, such as ultrasound elastography [5] and magnetic resonance elastography [6]. The resolution and imaging depth (0.5-2 mm) of OCE suggest that it may be useful for a range of applications, such as *in vivo* and *in situ* diagnostic imaging of superficial tissues in clinical environments [2].

OCE has undergone rapid development in recent years and has shown promise for applications in a number of areas, including oncology [7, 8], ophthalmology [9, 10] and cardiology [11, 12]. However, so far, OCE techniques have mainly been developed for proof-of-principle experiments in laboratory-based settings [2]. Translation of OCE towards clinical settings requires the tailoring of optical imaging systems and mechanical loading techniques for specific applications. For example, *in vivo* and intraoperative applications typically require rapid acquisition of elastograms, to avoid motion artifacts, and to ensure that elastograms are acquired within clinically relevant timeframes. Furthermore, certain applications, such as tumor margin assessment in breast-conserving surgery, require the acquisition of data over a surface area exceeding the typical field-of-view of OCE ($\sim$ 10$\times$10 mm) to ensure adequate sampling of the tissue [8]. For example, lumpectomy specimens excised during breast-conserving surgery can have a surface area up to $\sim$50 cm^2 [13]. To ensure that sufficient tissue is scanned, multiple OCE superficial volumes must be acquired from a single sample. A challenge in achieving this in clinically relevant timeframes is the time required, not only to acquire multiple volumes, but also to reposition the sample for each acquisition [14]. One potential solution is to increase the scanning speed of OCE, for example, by using a Fourier-domain mode-locked laser, as has been demonstrated in wave-based OCE [15]. Another approach to reducing acquisition time is to acquire multiple scans of the sample simultaneously, which has not yet been demonstrated.

In this letter, we propose a novel approach to phase-sensitive, compression OCE that enables elastograms to be acquired from two opposing surfaces of a sample simultaneously. Data acquired from the two surfaces are encoded with different carrier frequencies in the interferogram, resulting in non-overlapped depth-ranging from both surfaces after inverse Fourier transformation. This is achieved using a spectral-domain (SD) OCT system that incorporates two interferometers and a single spectrometer. A single loading device is applied to one side of the sample, allowing the same preload strain to be induced on two opposite sample surfaces. This approach, which we term depth-encoded OCE, is related to techniques previously proposed for simultaneous imaging of the anterior segment and retina in ophthalmic OCT [16] and for simultaneous transmission of multiple polarization states in polarization-sensitive (PS) OCT [17, 18]. To demonstrate depth-encoded OCE, we performed imaging on a silicone phantom containing stiff inclusions embedded in a soft matrix and on a sample of freshly excised mouse liver. The elastogram quality obtained is shown to be comparable to that achieved in single-sided compression OCE.

The optical layout of the depth-encoded OCE system is shown in Fig. 1(a). The light source is a superluminescent diode (SLD) (Superlum, Ireland) with a central wavelength of 835 nm and a 3-dB bandwidth of 50 nm. The sensitivity of the system was measured to be 102 dB at an exposure time of 36 μs and the displacement sensitivity was measured to be 0.34 nm for a corresponding OCT SNR of 50 dB [7]. The sensitivity roll-off of the spectrometer is -13 dB at 90% of the full axial range. The light from the SLD is split by a fiber coupler (FC) into a common-path interferometer and a dual-arm interferometer, with each shown by the shaded areas in Fig. 1(a). We positioned the sample arm of each interferometer to illuminate opposite sides of the sample through galvanometer-scanned mirrors (GSMs) and objective lenses (OLs) (Thorlabs LSM03-BB). The OLs provide a lateral resolution (FWHM of intensity) of 11 μm. The lateral scanning range is 4 mm $\times$ 4 mm on

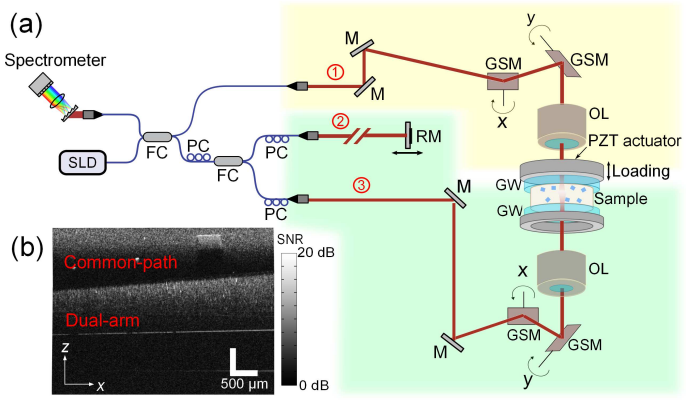

Figure 1: (a) Depth-encoded OCE setup using two interferometers to acquire signals from opposite sides of the sample simultaneously. The light-yellow area and light-green area indicate the common-path and dual-arm interferometers, respectively. The optical paths of the common-path interferometer, and reference and sample arms of the dual-arm interferometer are labeled 1, 2 and 3, respectively. Components: SLD, superluminescent diode. PC, polarization controller. FC, fiber coupler. GW, glass window. OL, objective lens. GSM, galvanometer-scanned mirror. M, mirror. RM, reference mirror. (b) OCT B-scan of a silicone phantom containing stiff inclusions acquired with the depth-encoded OCE system, showing images generated simultaneously from opposite sides of the sample.

each sample side, with a total scanning time of ∼10 minutes. The backscattered light collected by the sample arms of these two interferometers is detected by a single spectrometer. The reference optical path-lengths in the two interferometers are offset using fiber patch cords by ∼200 mm (far exceeding the coherence length of the light source) to avoid crosstalk interference between beams in the two interferometers. To ensure the backscattered light from both interferometers is mapped by the spectrometer without overlap within the imaging depth, the position of the reference mirror (RM) is shifted by ∼1 mm from the position matching the path-length to the sample surface in the sample arm of the dual-arm interferometer. Using this approach, the path-length difference between reference and sample arms is different for each interferometer, thus, ensuring different carrier frequencies in the spectral interferogram and avoiding spatial overlap in the resulting OCT A-scan acquired after implementation of an inverse Fourier transformation. In addition, to avoid unwanted common-path interference from the glass-sample interface in the dual-arm interferometer, the scan head is tilted by $\sim 10^\circ$ with respect to the sample surface. Thus, the B-scan image acquired using the dual-arm interferometer appears tilted by $\sim 10^\circ$ in the x-z plane, as shown in the lower part of Fig. 1(b).

Mechanical loading is performed by an annular PZT actuator in the common-path interferometer after the objective lens, as shown in Fig. 1(a). A glass window is fixed to the actuator surface both to allow light to be incident on the sample and to act as a compression plate. A glass window is also placed in the dual-arm interferometer and is fixed to rigid optomechanics. The sample is placed between the two glass windows and preloaded to ensure good contact. The actuator provides step-wise micro-scale compression of the sample synchronized with OCT B-scans. The

actuator introduces the same preload strain to both sample surfaces, assuming a mechanically uniform sample and the same friction at both sample surfaces. The sample's axial displacement in response to compression is measured using phase-sensitive detection described in detail previously [19, 7]. The local axial strain is calculated as the change in axial displacement with depth over axial ranges of 50 μm at each pixel in the dataset, using a weighted least squares method described previously [19]. Two 3D strain elastograms from opposite sides of the sample are then generated.

We performed measurements on a silicone phantom containing stiff inclusions [20]. The phantom is fabricated from two-part room temperature vulcanizing silicone, comprising bulk material (Wacker P7676, part A:B mixing ratio 1:1, elastic modulus: 13-20 kPa) and stiff inclusions (Wacker RT601, part A:B mixing ratio 5:1, elastic modulus: 275-338 kPa). The phantom has a cylindrical shape with a diameter of 10 mm and a thickness of 3 mm. The cubic inclusions in the phantom have a size of 400 μm and are embedded 100 - 300 μm from each of the two circular surfaces of the phantom. To introduce optical scattering, titanium dioxide particles are added, with a concentration of 3 mg/ml for the inclusions, and a concentration of 0.8 mg/ml for the bulk material. An example OCT B-scan of the silicone phantom, acquired with this depth-encoded OCE system, is displayed in Fig. 1(b), showing that both sides of the sample are imaged simultaneously. The OCT image acquired by the dual-arm interferometer in Fig. 1(b) exhibits significant optical dispersion. In Figs. 2 - 4, the results are displayed after dispersion compensation in post-processing, using a technique described in [21, 22].

We first demonstrate depth-encoded OCE on the silicone phantom described above. The results are shown in Figs. 2 and 3. In Figs. 2(a) - (c), OCT, phase difference and strain elastogram B-scans on both sample sides are shown for the same spatial location. In each figure, the lower image acquired from the dual-arm interferometer appears tilted by $\sim 10^\circ$ and an inclusion at the upper phantom surface is clearly observed. There is one horizontal line shown in Figs. 2(a) - (c), which is caused by internal back-reflections within the interferometers. In Figs. 3(a) and 3(b), an *en face* OCT image and strain elastogram of the top phantom surface, imaged by the common-path interferometer, are shown at a physical depth of 250 μm, indicated by the upper dashed lines in Figs. 2(a) - (c). In both the OCT image and strain elastogram, two inclusions are clearly visible. In Figs. 3(c) and 3(d), an *en face* OCT image and strain elastogram of the bottom phantom surface are shown. To generate the *en face* images, the OCT and strain elastogram B-scan images of the bottom phantom surface are tilted by $\sim 10^\circ$ in post-processing to compensate for the angle introduced experimentally. The *en face* images in Figs. 3(c) and 3(d) correspond to a depth of 200 μm, indicated by the lower dashed lines in Figs. 2(a) - (c). In both the OCT image and strain elastogram, an inclusion is clearly visible. The *en face* strain elastograms in Figs. 3(b) and 3(d) are averaged over a depth range of 150 μm, centered at the corresponding imaging depths on both sample sides, to increase strain contrast. The contrast in the OCT images and strain elastograms presented in Figs. 2 and 3 decays compared to our previous results using single-sided compression OCE [19, 7], due to an OCT sensitivity penalty for the spectrometer roll-off and for excess shot noise in this system. The strain sensitivity, which is defined in [19], is 0.9 mε in both top and bottom strain elastograms.

To demonstrate the feasibility of depth-encoded OCE of biological tissue, we scanned a freshly excised sample of mouse liver, comprising regions of stromal tissue interspersed with dense regions of blood clots. OCT images and strain elastograms were measured simultaneously for two opposite sides of this sample. As it was challenging to determine the exact scanning region of OCE, we added a white arrow in each of the photographs 4(c) and 4(f) to indicate the approximate location of the region scanned. The *en face* OCT images in Figs. 4(a) and 4(d) correspond to a depth of 50

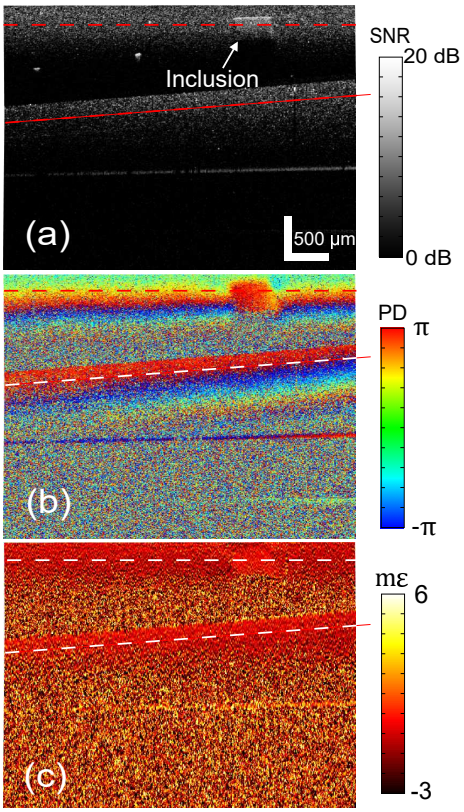

Figure 2: Phantom results. (a) OCT B-scan. (b) Phase difference (PD) B-scan. (c) Strain elastogram B-scan, in units of millistrain (mε). The top part of each image, *i.e.*, starting at the zero path-length delay, represents the top surface of the phantom and was acquired with the common-path interferometer. The tilted lower part of each image represents the bottom surface of the phantom and was acquired with the dual-arm interferometer. The dashed lines indicate the depths corresponding to the *en face* images in Fig. 3. All the subfigures have the same scale bar.

μm below the tissue surface. The *en face* strain elastograms, Figs. 4(b) and 4(e), are averaged over a depth range of 150 μm from the sample surface. The OCT image and strain elastogram acquired from the top surface of the tissue are presented in Figs. 4(a) and 4(b), along with the corresponding photograph in Fig. 4(c). In the top right region of the elastogram, a region of heterogeneous strain is labeled by white arrows, which likely corresponds to a region of blood clots such as the one near the white arrow in the photograph (Fig. 4(c)). We believe that this heterogeneity originates both from mechanical heterogeneity in blood clots, as well as from OCT signal decorrelation caused by Brownian motion. By comparison, the region corresponding to the liver tissue surrounding the blood clots has a more homogeneous strain signature, as would be expected from the more uniform mechanical properties of liver tissue. The OCT image and strain elastogram acquired from the bottom of the sample, along with the corresponding photograph, are shown in Figs. 4(d) - 4(f). A similar strain pattern to that of the top surface, again indicated by white arrows, is observed.

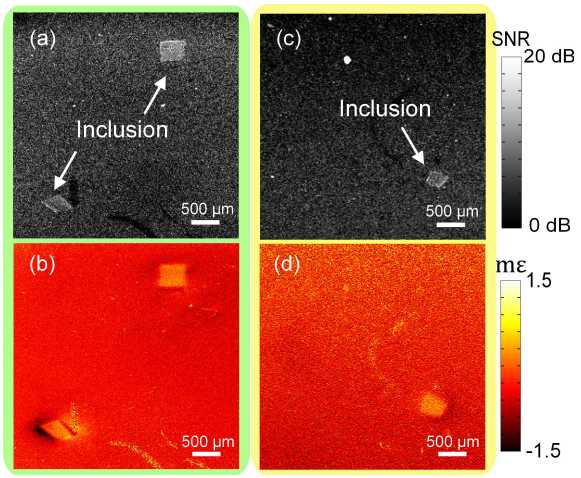

Figure 3: *En face* phantom images. The *en face* image depths shown here are indicated by the dashed lines in Fig. 2. (a) OCT image and (b) strain elastogram of the top surface of the sample. (c) OCT image and (d) strain elastogram of the bottom surface of the sample.

A region to the left of Fig. 4(e) highlighted by white arrows, possibly corresponding to a region containing blood clots such as the one near the white arrow in Fig. 4(f), presents a heterogeneous strain signature, whilst a region of surrounding liver tissue to the right of the image presents a more uniform strain pattern.

The use of depth-encoded OCE halves the scanning time of the sample for applications such as breast-conserving surgery, where multiple surfaces of a tissue sample need to be scanned rapidly. Importantly, this technique also reduces the time burden of placing and pre-loading the sample multiple times. The use of a single spectrometer maintains the detection hardware for scanning multiple volumes simultaneously equal to that of a single-sided approach and is, thus, also more amenable to compact imaging systems, ultimately required for clinical deployment of OCE. Also, importantly for clinical applications, as two OCT A-scans are effectively generated from one inverse Fourier transformation operation, our technique has the potential to reduce the signal processing time, if hardware dispersion compensation is implemented, as two OCE volumes are obtained from one 3D complex OCT dataset.

In our depth-encoded OCE system, the sample is scanned from opposite surfaces. The two-interferometer setup ensures that displacements are estimated from both sides of the sample simultaneously. In principle, any two surfaces of the sample, not necessarily opposite to one another, can be scanned by changing the optical setup and loading method. For example, we can implement two common-path interferometers and two PZT actuators to measure elastograms from two surface areas on one sample side. To do this, two glass windows incorporating reference arms of different lengths would need to be realized to avoid carrier frequency overlap between the two interferometers.

In conclusion, we have presented a depth-encoded OCE system that can acquire volumetric strain elastograms from two sides of the same tissue sample simultaneously. This system is realized by selecting optical path-lengths in the two interferometers such that depth-ranging from both interferometers can be measured simultaneously using one spectrometer. We demonstrated the feasibility of depth-encoded OCE on a silicone phantom with stiff inclusions and on a specimen of

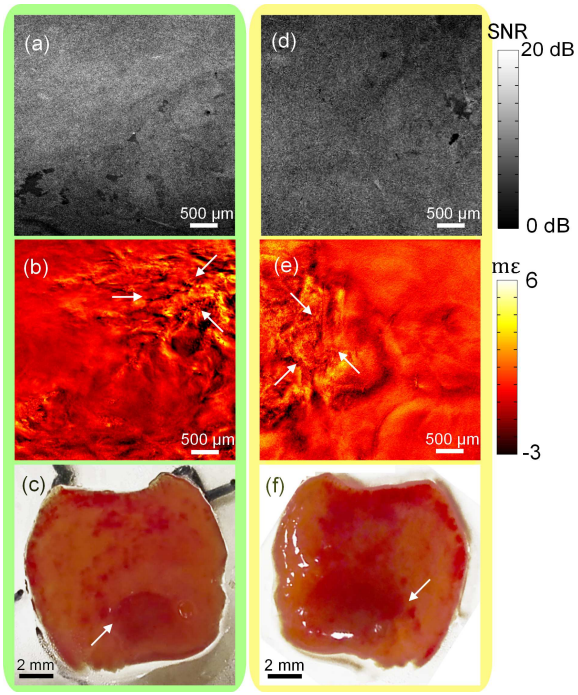

Figure 4: Results from a freshly excised sample of mouse liver. (a) *En face* OCT and (b) strain elastogram of the top surface, respectively, acquired with the common-path interferometer. (d) *En face* OCT and (e) strain elastogram of the bottom surface, respectively, acquired using the dual-arm interferometer. (c) and (f) are photos of the top and bottom sides of the liver sample, respectively. The arrows in (b) and (e) indicate heterogeneous areas in the strain elastograms, which are likely to correspond to blood clots in the photos, indicated by white arrows in (c) and (f).

freshly excised mouse liver. We anticipate that depth-encoded OCE could prove to be an important tool to expedite the translation of OCE to intraoperative applications.

Funding. This research was supported by grants from the Australian Research Council, the National Health and Medical Research Council (Australia), the National Breast Cancer Foundation (Australia), and the Department of Health, Western Australia.

References

[1] J. M. Schmitt, Opt. Express **3**, 199 (1998).

[2] B. F. Kennedy, K. M. Kennedy, and D. D. Sampson, IEEE J. Sel. Top. Quantum Electron. **20**, 7101217 (2014).

[3] K. Larin and D. D. Sampson, Biomed. Opt. Express **8**, 2 (2017).

[4] H.-J. Butt, B. Cappella, and M. Kappl, Surf. Sci. Rep. **22**, 1 (2005).

[5] A. P. Sarvazyan, O. V. Rudenko, S. D. Swanson, J. B. Fowlkes, and S. Y. Emelianov, Ultrasound Med. Biol. **24**, 1419 (1998).

[6] R. Muthupillai and R. L. Ehman, Nat. Med. **2**, 601 (1996).

[7] B. F. Kennedy, R. A. McLaughlin, K. M. Kennedy, L. Chin, A. Curatolo, A. Tien, B. Latham, C. M. Saunders, and D. D. Sampson, Biomed. Opt. Express **5**, 2113 (2014).

[8] B. F. Kennedy, R. A. McLaughlin, K. M. Kennedy, L. Chin, P. Wijesinghe, A. Curatolo, A. Tien, M. Ronald, B. Latham, C. M. Saunders, and D. D. Sampson, Cancer Res. **75**, 3236 (2015).

[9] S. Wang and K. V. Larin, Opt. Lett. **39**, 41 (2014).

[10] C. Li, G. Guan, Z. Huang, M. Johnstone, and R. K. Wang, Opt. Lett. **37**, 1625 (2012).

[11] W. Qi, R. Li, T. Ma, J. Li, K. K. Shuang, Q. Zhou, and Z. Chen, Appl. Phys. Lett. **103**, 103704 (2013).

[12] G. van Soest, F. Mastik, N. de Jong, and A. F. W. van der Steen, Phys. Med. Biol. **52**, 2445 (2007).

[13] T. L. Huston, R. Pigalarga, M. P. Osborne, E. Tousimis, Am. J. Surg. **192**, 509 (2006).

[14] W. M. Allen, L. Chin, P. Wijesinghe, R. W. Kirk, B. Latham, D. D. Sampson, C. M. Saunders, and B. F. Kennedy, Biomed. Opt. Express **7**, 4139 (2016).

[15] M. Singh, C. Wu, C. Liu, J. Li, A. Schill, A. Nair, and K. V. Larin, Opt. Lett. **40**, 2588 (2015).

[16] A. Dhalla, D. Nankivil, T. Bustamante, A. Kuo, and J. A. Izatt, Opt. Lett. **37**, 1883 (2012).

[17] C. E. Saxer, J. F. de Boer, B. H. Park, Y. Zhao, Z. Chen, and J. S. Nelson, Opt. Lett. **25**, 1355 (2000).

[18] Z. Wang, H-C Lee, O. O. Ahsen, B. Lee, W. Choi, B. Potsaid, J. Liu, V. Jayaraman, A. Cable, M. F. Kraus, K. Liang, J. Hornegger, and J. G. Fujimoto, Biomed. Opt. Express **5**, 2931 (2014).

[19] B. F. Kennedy, S. H. Koh, R. A. McLaughlin, K. M. Kennedy, P. R. T. Munro, and D. D. Sampson, Biomed. Opt. Express **3**, 1865 (2012).

[20] G. Lamouche, B. F. Kennedy, K. M. Kennedy, C. E. Bisaillon, A. Curatolo, G. Campbell, V. Pazos, and D. D. Sampson, Biomed. Opt. Express **3**, 1381 (2012).

[21] A. F. Fercher, C. K. Hitzenberger, M. Sticker, R. Zawadzki, B. Karamata, and T. Lasser, Opt. Express **9**, 610 (2001).

[22] M. Wojtkowski, V. J. Srinivasan, T. H. Ko, J. G. Fujimoto, A. Kowalczyk, and J. S. Duker, Opt. Express **12**, 2405 (2004).